SEMINÁRIOS PPG-EM / UERJ 2022

PPG-EM UERJ 2022 SEMINARS

Programa de Pós-graduação em Engenharia Mecânica UERJ

Graduate Program in Mechanical Engineering UERJ

SEMINÁRIOS PPG-EM / UERJ 2022

PPG-EM UERJ 2022 SEMINARS

Programa de Pós-graduação em Engenharia Mecânica UERJ

Graduate Program in Mechanical Engineering UERJ

WWW.PPGEM.UERJ.BR

May 17, 2023

Sumário / Contents

1. Mini-artigos / Short papers

17 de maio de 2023

Neste capítulo são apresentados os mini-artigos dos onze trabalhos científicos que fizeram parte dos Seminários do PPG-EM em 2022. Os trabalhos estão organizados segundo a data de apresentação.

Prof. Daniel J. N. M. Chalhub, D.Sc.
Coordenador dos Seminários PPG-EM 2022

May 17, 2023

This chapter presents the short papers of the eleven scientific papers that participated in the PPG-EM Seminars in 2022. Papers are organized according to the date of presentation.

Prof. Daniel J. N. M. Chalhub, D.Sc.
PPG-EM 2022 Seminars Chair

HEAT TRANSFER IN NON-CONVEX BODIES

Author: Allan Moraes de Lira[1] *allanmoraesdelira@gmail.com*
Advisor(s): Rogério M. S. da Gama [1] Maria Laura Martins Costa[2]
[1]Rio de Janeiro State University ; [2]Federal Fluminense University

Keywords: Heat transfer, thermal radiation, thermal conduction, non-Convex Body.

1 Introduction

This work aims to present computer simulations that show that the temperature field of a non-convex body, when subjected to heat transfer, changes significantly when the effects of non-convexity of the body are considered. To accomplish this purpose, the problem of heat transfer, in steady state, was approached in a black body considered rigid, flat, continuous, non-convex, opaque, at rest, with a high temperature boundary, with constant thermal conductivity and that has a known internal power generation. The medium in which this body is located is considered non-participant, and therefore the effects of convection are neglected. This problem is mathematically characterized by an elliptic partial differential equation with nonlinear boundary condition, as it represents the coupling of energy transfer by conduction, which occurs inside the body, with the transfer of energy by thermal radiation which occurs at the boundaries of the body. , in addition to the fact that the body is not convex. The processes of energy transfer in bodies at high temperatures, in which it is necessary to consider the coupling of conduction with radiation, are present in several fields of science and industry, such as, for example, the study of heat transfer in artificial satellites.
A body is considered non-convex when it has the property of being a source of thermal radiation from itself [5]. The boundary condition for a non-convex body contains the shape factor of the body, dependent only on its geometry, and represents the fraction of the radiation that leaves a part of the surface of the body that impinges on another part of the same body [5].
An example of application of the effects of non-convexity of a body is to improve the efficiency of solar collectors. The V-groove solar collector is more advantageous because of the non-convexity of its surface parts [5].

2 Theoretical foundation

The mathematical description for the conservation of energy with respect to a continuous, rigid, at rest and opaque body can be summarized as follows:

$$\rho c\, \partial T/\partial t = -div\mathbf{q} + \dot{q} \quad em\ \Omega \qquad (1)$$

where c is the specific heat, considered constant, T represents the temperature field of the rigid body, ρ is the density, $\mathbf{q}$ is the heat flux vector (per unit time and area) and $\dot{q}$ is the rate of internal heat generation (per unit time and volume).
It is known that Fourier's Law is given, expressed in rectangular Cartesian coordinates, by the following equation

$$\mathbf{q} = -k(\partial \mathrm{T}/\partial \mathrm{x}\, \hat{\boldsymbol{\imath}} + \partial \mathrm{T}/\partial \mathrm{y}\, \hat{\boldsymbol{\jmath}} + \partial \mathrm{T}/\partial \mathrm{z}\, \hat{\boldsymbol{k}}) \quad em \quad \Omega \qquad (2)$$

Where k is a thermal transport property called thermal conductivity, and depends on the physical structure of matter, atomic and molecular. Applying Fourier's law to equation (1), we have that

$$\rho c\, \partial T/\partial t = div(k\,\mathrm{grad\ T}) + \dot{q} \quad em \quad \Omega \qquad (3)$$

For the case that heat conduction occurs in a steady state and the thermal conductivity is constant, we have that

$$div(\mathrm{grad\ T}) + (\dot{q}/k) = 0 \quad em \quad \Omega \qquad (4)$$

Equation (4) governs heat conduction in a rigid, isotropic, opaque body, at rest and in steady state, and requires boundary condition, given by

$$-k\, grad\, T \bullet \boldsymbol{n} = \sigma|T|^3 T - \int \sigma|T(y)|^3\, T(y) K(x,y) dS, \partial\Omega \qquad (5)$$

More details about the boundary condition described by (5) can be found in reference [3].

The computer simulations of the heat transfer process, in steady state, in a non-convex black body, which compare the temperature fields considering the non-convexity of the body and disregarding the effects of the non-convexity of the body, will be given through the solution of this problem: consider the heat transfer, in steady state, in a plate, homogeneous, considered a blackbody, non-convex, opaque, at rest and with constant thermal conductivity. The medium in which the plate is contained is considered to be non-participating, so there is no convection. Furthermore, it is assumed that the board has a known constant internal energy generation. $\dot{q}$ corresponding, for example, to a microchip where heat dissipation occurs due to the passage of an electric current. The region occupied by the plate is represented by Ω, and its borders are represented by $\partial\Omega$. This problem is illustrated in the figure below.

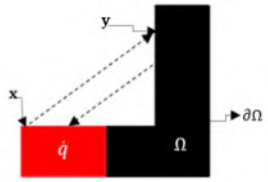

Figure 1. Homogeneous, non-convex rigid plate, considered a black body that occupies a flat region Ω and borders $\partial\Omega$. The horizontal region in red represents the internal power generation $\dot{q}$.

Equations (4) and (5) model the problem illustrated by figure 1, with the value of $K(\boldsymbol{x},\boldsymbol{y})$, present in equation (5), for the plate of figure 1, given by

$$K(x,y) = \frac{xy}{2(x^2+y^2)^{3/2}} \qquad (6)$$

where K$(\boldsymbol{x},\boldsymbol{y})$ is called the form factor. The form factor depends only on the geometry of the cup, and represents the fraction of the radiation that leaves a part of the surface of the body that impinges on another part of the same body [23].

The method used to solve The problem illustrated in figure 1 and modeled by equations (4), (5) and (6), as well as the entire procedure to obtain the computer simulations can be found in reference [3].

3 Results

The simulation results are as follows:

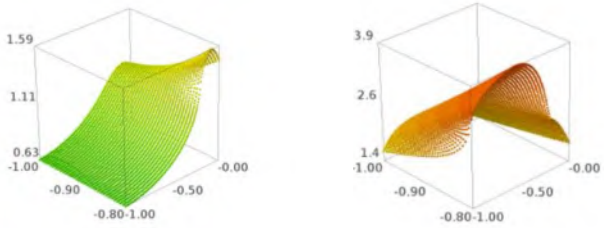

(a) (b)

Figure 2. (a) 160 x 160 mesh. Temperature field on the vertical side of the plate, without the effects of non-convexity. (b) 160 x 160 mesh. Temperature field on the vertical side of the plate, with the effects of non-convexity.

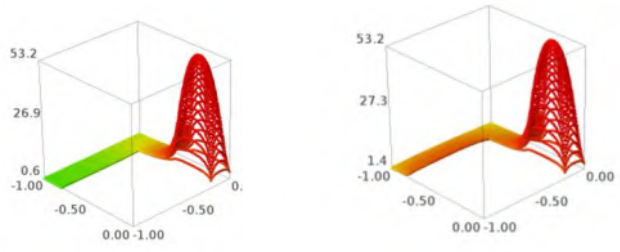

(a) (b)

Figure 3. (a) 160 x 160 mesh. Plate temperature field, without non-convexity effects. (b) Mesh 160 x 160. Plate temperature field, with non-convexity effects.

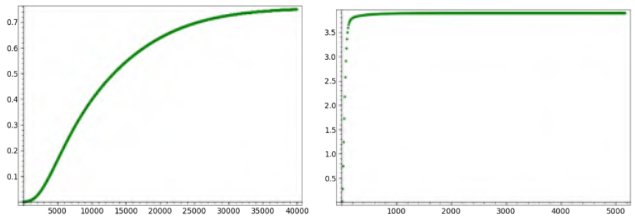

(a) (b)

Figure 4. (a) Mesh 160 x 160. Temperature of the midpoint of the vertical side of the plate that communicates with its horizontal side, without the effects of non-convexity. (b) Mesh 160 x 160. Temperature of the midpoint of the vertical side of the plate that communicates with its horizontal side, with the effects of non-convexity.

4 Final Considerations

The computer simulations presented in this work show that when the effects of non-convexity are neglected, the temperature levels are significantly lower when compared to the temperatures considering the effects of non-convexity.

5 References

[1] Gama, R.M.S. On a class of elliptic problems and its application to heat transfer in nonconvex bodies. Journal of Computational Mathematics, vol.11, no.4, pp.301-312, 1993.

[2] Gama, RMS.; Fundamentos de mecânica dos fluidos, ed UERJ, Rio de Janeiro, 2012.

[3] Lira, Allan Moraes de. Simulação computacional do processo de transferência de calor em regime permanente, com condições de contorno não lineares, a partir de uma sequência de problemas lineares / Allan Moraes de Lira. – 2022.

[4] Gama, R.M.S. A new mathematical model for energy transfer problems with radiative boundary conditions. Applied Mathematical Modelling, no.2, vol.14, pp.96-103, 1990.

[5] Gama, R.M.S. Existence, uniqueness and construction of the solution of the energy transfer problem in a rigid and non-convex blackbody with temperature-dependent thermal conductivity. Z. Angew. Math. Phys. 66, (2015).

PPG-EM
Programa de Pós-graduação em Engenharia Mecânica

COMPARATIVE ANALYSIS BETWEEN COMPUTED TOMOGRAPHY AND 3D RECONSTRUCTION TECHNIQUES OF OPTICAL MICROSCOPY IMAGES IN THE POROSITY QUANTIFICATION OF HIGH HARDNESS ADVANCED CERAMICS

Author: Vinicio Coelho da Silva[1] *viniciorj@hotmail.com*
Advisor(s): Marilia Garcia Diniz[1]
[1] Rio de Janeiro State University

May 17, 2022
PPG-EM Seminars: season **2022**
http://www.ppgem.uerj.br

Keywords: Silicon Carbide, Boron Carbide, Porosity, Digital Image Processing, Computed Tomography.

1 Introduction

Silicon carbide (SiC) and boron carbide (B4C) are highlight of ceramic class. These materials have excellent mechanical properties at low and high temperatures, high wear resistance, high thermal stability and corrosion resistance. Their unique characteristics of them allow it to be used in various structural applications [1]. Some problems still limit the scope of silicon carbide, and other ceramics in general. The high cost of the manufacturing process, the difficulty of sintering and the control of porosity, with the difficulty of more complex geometries. There are effective techniques for the evaluation and quantification of the existing porosity in advanced ceramics, such as computed tomography, however, these techniques require high equipment and handling costs, which led to the search for alternatives that provide equally safe and less costly results, as quantitative stereology using the Digital Image Processing (DIP).

2 Methodology

Until now we used three silicon carbide samples with 10x10x11mm provided by ESK manufacturer, Ekasic F group [2]. These samples were submitted to Archimedes procedure for density measurements, according to the NBR 6220 ABNT [2]. They were embedded, ground and polished in nine layers (100, 200, 500, 1000, 2000, 3000, 4000, 5000, and 6000 uM) for obtaining optical microscopy images throughout the material. The following collection were 108 images of the surfaces of samples with an optical microscope (MO) Olympus BX60M, 36 for each sample (04 in each of the nine sections) in different regions of the surface. All were collected under 100x magnification. The digital image processing was carried out through AxionVision software [2]. All images were processed individually and involved steps of preprocessing, segmentation and feature extraction. There was no need to eliminate "noise" and lighting correction to generate bimodal histograms for images.

3 Results and Discussion

In the case of commercial samples, the manufacturer claims that the porosity of the material is less than 2.0 percent of its volume and density is 3,15g/cm3. Figures 01 and 02 respectively illustrate an image obtained by an increase of MO 500X and the result after the segmentation step for extracting attributes and quantifying the number of pores (light dots in Figure 2). Table 1 shows the porosity obtained by DIP. Table 2 shows the densities obtained using the Archimedes method.

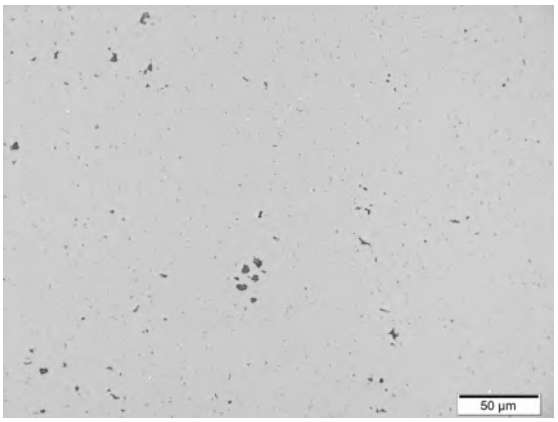

Figure 1

Table 1: Porosities obtained by DIP.

	percentage value
Porosity of sample 01	0,622
Porosity of sample 02	0,606
Porosity of sample 03	0,579
Average porosity of the material	0,602

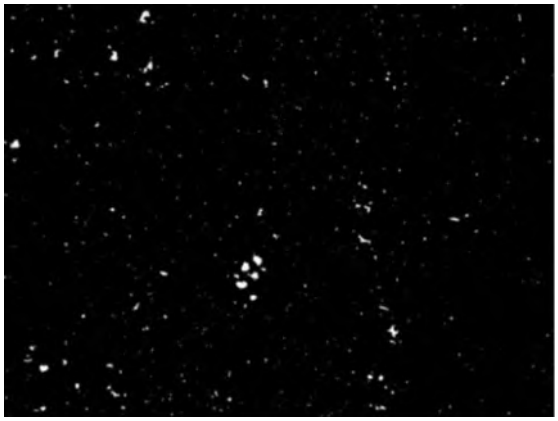

Figure 2

Table 2: Densities obtained by the Archimedes method.

Bulk density (g/cm3)	Relative Density	Relative Density (percentage)
3,09	0,98	98,09
3,15	1,00	100,00
3,16	1,00	100,00
3,17	1,00	100,00
Average porosity (percentage)	0,48 (+ - 0,82)	

4 Conclusions

It was found that the percentage of porosity found for the methods by Archimedes and PDI showed a great similar- ity (0.48 percent with variation of 0.82 by Archimedes and 0.6 percent with variation of 0.018 per PDI) and did not exceed the 2.0 limit percentual stipulated by the manufacturer for ESK lot Ekasic F SiC. A detailed procedure has been prepared that will serve as a guide for future research. The digital image processing was credibility stated for the tested samples, proved to be a suitable method which is based on quantitative metallographic procedures.

5 Acknowledgments

The author thanks the UFRJ Advanced Ceramics Laboratory for providing the material to carry out this research.

References

[1] G. S. ABREU. *Sinterização em alta pressão e alta temperatura (HPHT) do compósito B4C-Nb.* Tese de doutorado, UENF, Campos dos Goytacazes - RJ, 2019.

[2] Vinicio Coelho da Silva. Medida de porosidade em sic atraves de processamento digital de imagens. Master's thesis, UERJ, abril 2015.

[2] [1]

PPG-EM
Programa de Pós-graduação em Engenharia Mecânica

NONDETERMINISTIC DYNAMIC ANALYSIS AND STRUCTURAL OPTIMIZATION OF THE STEEL TOWERS DESIGN FOR WIND TURBINES SUPPORT

Author: André Victor da Silva Castilho[1] *andrevictor_castilho@hotmail.com*
Advisor(s): José Guilherme Santos da Silva, Francisco José da Cunha Pires Soeiro[1]
[1] Rio de Janeiro State University

PPG-EM Seminars: season **2022**
http://www.ppgem.uerj.br
May 17, 2022

Keywords: Wind towers, Dynamic Structural Analysis, Structural optimization.

1 Introduction

Due to the growing demand for electricity in addition to the need to reduce the emission of greenhouse gases, the adoption of energy from renewable sources has shown significant growth. Due to its technological development and competitive prices, the use of wind energy has raised its installed capacity around the world in recent years. According to [1], Brazil currently has 21.5 GW of installed wind power, with 795 wind farms, more than 9000 wind turbines in operation in 12 states of the federation, with an estimated increase in its installed power to 24.2 GW by the end of the year 0f 2024. This development of the wind sector is justified by the quality of the winds, which present considerable stability, without sudden variations in speed and direction.

In the installation of a wind farm, the construction of steel towers to support the wind turbines represents a significant part of its total cost. Such structures represent 20 to 30% of the total cost of a wind turbine, thus, obtaining optimized designs represents a valid approach to reduce the cost of installing these devices [2]. In this context, this work aims to carry out a structural analysis of a steel tower to support a Repower MM92 wind turbine with a production capacity of 2 MW, for further optimization of the structural design using genetic algorithms.

2 Methodology

The analyzed structure consists of a conical steel tower 76 meters tall with a variable thickness along its height, with 30 mm at its base and 12 mm at the top, with an opening at the bottom. The nacelle is located at its top and a reinforced concrete foundation is located at its bottom. The structure was modeled in finite elements using APDL (Ansys Parametric Design Language) and and its finite element model is presented in Figure 1. This model considers the wind action along the tower through the simplified continuous method as proposed in [3]. The wind forces on the rotor are interpolated for a 2 MW turbine [4]. It is also considered the interaction between soil and structure from an average soil stiffness as proposed in [5]. The non-deterministic action of the wind for the transient analysis is modeled using the Kaimal's power spectrum, and due to this nature, in the dynamic analyzes statistical treatments are carried out in order to obtain displacement and stress values considering a confidence level of 95%.

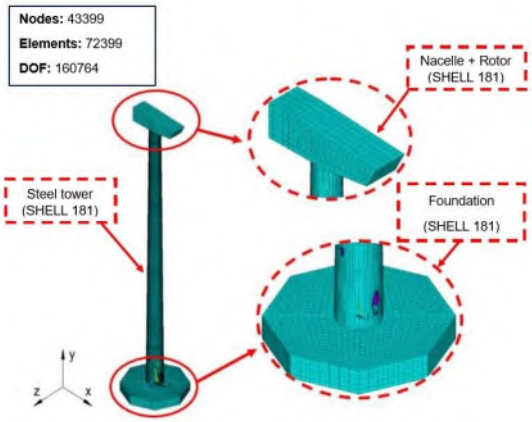

Figure 1: Finite element model for the MM92 wind turbine support tower.

The structural optimization in this work is performed through genetic algorithms, with an interaction between Ansys and MATLAB software, in order to minimize the total volume of the steel tower. This procedure can be briefly described by the following steps:

1. The algorithm creates a random population
2. This population serves as input parameters for ANSYS which runs in batch mode generating output data
3. MATLAB checks the results in the output files and then checks the design constraints
4. If the conditions are satisfied, MATLAB accept the new volume, otherwise it is discarded
5. This process repeats until the stopping criterion is reached.

After this process, the algorithm obtains the combination of design variables that result in the smallest

volume for the steel tower, complying with all design constraints.

3 Structural Optimization

The optimization problem given in this work aims to reduce the total volume of the steel tower for wind turbine support. For this, the tower is divided into three different sections and at their interface the thicknesses are checked and taken to define the project variables vector: $X = [EA\ EB\ EC\ ED]$. The problem is taken considering two project restrictions: the maximum displacement at the top of the tower; and its maximum von Mises stress as presented in [6]. Thus, the optimization problem must be given in order to minimize:

$$f(X) = V_{Tower} \tag{1}$$

subject to the inequality constraints:

1. Displacement restriction:

$$\delta_{Max} \leq 1.52m \tag{2}$$

2. Stress restriction:

$$\sigma_{Max} \leq 263MPa \tag{3}$$

4 Results and Discussions

For all analyzes presented here, a basic wind speed of 50 m/s is considered. This value was selected because it is the highest basic wind speed value in Brazil, in its southern region.

Table 1: Thicknesses and volume for the support tower, with initial and optimized values.

	Inicial Value	Optimum Value
EA	30 mm	24 mm
EB	26 mm	21 mm
EC	16 mm	12 mm
ED	12 mm	8 mm
Volume	17.7 m^3	13.8 m^3

Initially, a static analysis is performed using the simplified continuous model for the wind load. For this case, the tower presents a maximum stress of $209MPa$ at its bottom opening and a displacement of $1.125m$ at the top. After this, an optimization through genetic algorithm is performed in order to get the new project variables and optimized volume. The results are presented in Table 1. As shown, the thicknesses along the tower were reduced considerably, resulting in a 23% reduction in its total volume.

Observing the values for the design constraints presented in Table 2, it can be seen that the maximum displacement value at the top of the tower after the optimization represents 98.6% of the admissible value. This shows that the algorithm can satisfactorily approach the design constraints.

Table 2: Project restriction values.

	Restriction Value	Optimum Value
δ_{Max}	1.52 m	1.50 m
σ_{Max}	263 MPa	233 MPA

For the dynamic analysis, thirty series of non-deterministic wind loading by the Kaimal's power spectrum were considered. After the statistical treatment of the data, were obtained a maximum stress of $211MPa$ and a displacement of $1.33m$ on the top of the tower. This displacement value highlights the need to consider this loading in the conception of the optimization of the tower design, representing 12% more than the value obtained in the first analysis.

5 Conclusions

This work presents initial analyzes for the optimization through genetic algorithms for a steel tower wind turbine support using the interaction between ANSYS and MATLAB software. The analyzed model considers the wind action on the rotor, steel tower and its interaction with the ground. According to what was presented, it was possible to verify that the methodology presented was able to obtain a reduction of 23% in the total volume of the tower for the simplified continuous model. Such a reduction can be considered significant in the cost of implementing wind farms. However, for the consideration of non-deterministic wind loading on the tower, additional analyzes must be carried out for proper optimization.

References

[1] Associação Brasileira de Energia Eólica. Energia eólica: Os bons ventos do brasil. Technical report, ABEEólica, 2022.

[2] P. E. Yoshida. Wind turbine tower optimization method using genetic algorithm. *Wind Engineering*, 30, 2006.

[3] George Keith Batchelor. *NBR 6123: Forças devidas ao vento em edificações*. Associação Brasileira de Normas Técnicas, 1988.

[4] B. Shen G. Umut O., Akbas. Design issues of wind turbine towers. *International Conference on Structural Dynamics*, 8, 2011.

[5] Joseph E. Bowles. *Foundation analysis and design*. McGraw-Hill, 2001.

[6] *Design of Steel Structures, Parte 3-2, Tower, masts chimneys*. European Committee for Standardization, 2004.

PPG-EM
Programa de Pós-graduação em Engenharia Mecânica

STUDY OF GRAPHENE DEPOSITED ON INTERDIGITATED COPPER SUBSTRATE FOR AMMONIA GAS SENSING

Author: Eric Schwartz[1] *ericschwartzeng@gmail.com*
Advisor(s): Jose Brant[1]
[1] Rio de Janeiro State University

PPG-EM Seminars: season **2022**
http://www.ppgem.uerj.br
April 26, 2022

Keywords: Ammonia, Graphene, RGO, SEM

1 Introduction

Ammonia gas is widely used as a component in various industrial sectors (pharmaceuticals, plastics, chemicals, fertilizers, textiles, among others). As a corrosive, poisonous and highly toxic gas, ammonia can cause serious damage to the respiratory tract for humans, the nervous system, eyes, human skin and even death at high concentrations. Moreover, the exhaled breath of patients with kidney disorders and peptic ulcer releases NH3, in which it plays an important biomarker for diagnosis. Common ammonia sensors are made of metal oxides and must operate at high temperatures, leading to a high power consumption and reduced lifespan. To coup with this, graphene based sensors, able to operate at ambient temperature, has been proposed as an alternative to metal oxides.

2 Methodology

The devices were microfabricated in a process compatible with CMOS technology through a collaboration with the Catholic University of Louvain, Belgium. To observe the quality of the lithographic processing, in a scanning electron microscope (SEM) model JEOL-JSM-7100FT of NANOFAB/UERJ, the devices were individually separated by cleavage. The sample received an ultrasonic bath with acetone for 10 minutes followed by a second bath with isopropyl alcohol for 10 minutes and dried with an air jet to remove the polymer.

Graphene oxide (GO) was synthesized at LABMEQ/UERJ by the modified Hummer method and then thermally reduced at 600C for 1 min with a heating rate of 30C to obtain reduced graphene oxide (RGO). For characterization of the RGO were performed SEM images in JEOL-JSM-7100FT of NANOFAB/UERJ of RGO deposited on stub and fixed on carbon tape. For analysis of laser Raman spectroscopy was used Shamrock Spectrometer (iDus), Coherent Sapphire Laser (488nm). The measurements were performed with a beam exposure of 15min and power 400uW.Energy dispersive spectroscopy (EDS) was used for region mapping to investigate the chemical composition of RGO.

3 Results

Images taken with SEM in secondary electron mode show the device fabricated using the lithography method with well-defined morphology and dimensions with distance between the square-shaped measurement pads of area 202 x 202m and the region of the interdigitate with area 397 x 209 m (figure1.A). The enlarged red region in figure1.B demonstrates the constant morphology of the interdigitated pattern, with the spacing between the copper tracks having nearly identical dimensions, with little or no difference.

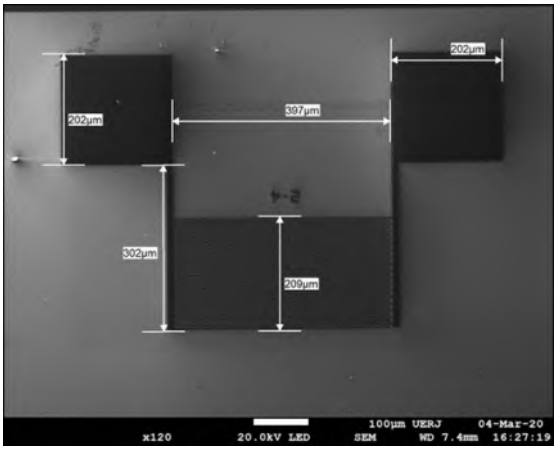

Figure 1: SEM images of the interdigitate morphology and its dimensions in secondary electron detection mode. Component image in (A) and in (B) magnification of the region in red k

To investigate the behavior of the copper tracks on the silicon oxide substrate, cross-section observation was performed with the backscattered electron mode (figure 2). It is observed that the copper trails with a thickness of 51nm, in lighter shades, seem to be at a slightly lower level than the silicon oxide of thickness 270nm. Below the silicon oxide is another substrate composed only of silicon on which its thickness was not obtained.

The morphology of the RGO sample was investigated using secondary electron mode SEM images. Figure 3.A shows RGO particles at 500x magnification as overlapping sheets due to the sample deposition process and

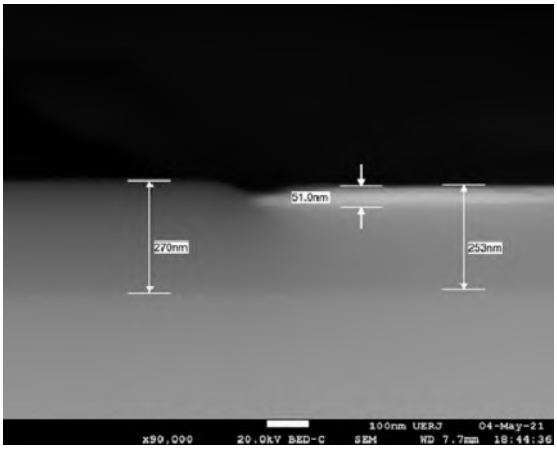

Figure 2: Backscattered electron SEM images of the cross-sectional view of the interdigitate and investigation of the copper track on the silicon oxide *k*

the natural tendency of RGO to stack. An observation of an RGO area at higher magnification (figure3.B) shows the characteristic appearance of an RGO sheet with flat areas, coming from the reduction of functional groups present in the GO, and areas with the presence of wrinkles and folds, attributed in the literature by the interaction of oxygenated groups on the surface.

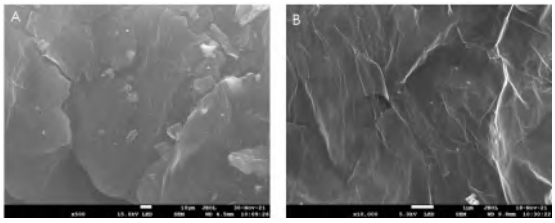

Figure 3: SEM images in secondary electron mode of the reduced graphene oxide at 500x magnification (A) and 10,000x magnification (B) *k*

The Raman spectrum of RGO (figure4) reveals the intensity of the D-band (1356), a band related to the presence of defects in the graphitic crystalline network, and the G-band (1590),band related to the bonds of carbons hybridized in the sp2 state.The ratio between the ID/IG intensities reveals the degree of defects in RGO has a value of 0.89, similar value are found in the literature, indicating the reduction of GO

Figure 5 shows the EDS spectrum performed on the RGO sample. The presence of only the C and O peaks show that the sample has no contamination from other elements, and the intensity of the peaks, with a C peak higher than the O peak, proves the reduction of GO.

4 Conclusions

The present work was able to characterize the standard morphology of the copper interdigitates and the morphological and chemical characteristics of the RGO, demonstrating that the synthesized RGO had similar ID/IG patterns and chemical composition to those

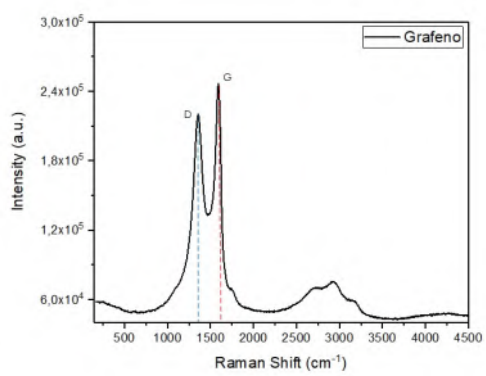

Figure 4: EDS chart demonstrating the chemical composition and providing a semi-quantitative analysis of the RGO *k*

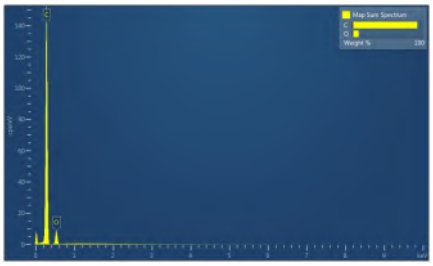

Figure 5: BRaman spectrum highlighting the D (blue) and G (red) bands of RGO *k*

presented in the literature. The next step for characterization will be the FTIR spectrum to obtain the oxygenated groups present and the construction of the conductivity curve and the recovery curve of the RGO deposited on the interdigitated pattern for adsorption of ammonia molecules.

5 Acknowledgments

The author thanks Prof. José Brant, Prof. Suzana Peripolli, Prof. Fernando Massa and the NANOFAB team for their support. Thanks to Prof. Deborah Vargas LABMEQ/UERJ team for the RGO made available and to the institution CBPF for the measurements in RAMAN and EDS.

References

[1] Benevides A, Campos A, Vieira L, dos Reis Perez C, Cesar D. Reduced graphene oxide-zinc oxide flower-like composite for glass-ionomer materials reinforcement. Materials Research, 23(1), 2020.

[2] L. G. Guex, B. Sacchi, K. F. Peuvot, R. L. Andersson, A. M. Pourrahimi,V. Ström, S. Farris and R. T. Olsson. Experimental review: chemical reduction of graphene oxide (GO) to reduced graphene oxide (rGO) by aqueous chemistry.Nanoscale, 9(27):9562-9571, 2017.

PPG-EM
Programa de Pós-graduação em Engenharia Mecânica

CONVECTIVE PATTERNS IN HELE-SHAW FLOWS DRIVEN BY CONCENTRATION GRADIENTS AND CHEMICAL COMPOSITION CHANGES

Author: Bernardo Alberto Marcussi[1] *lattes@uerj.br*
Advisor(s): Norberto mangiavacchi[1]
[1] Rio de Janeiro State University

May 15, 2022
PPG-EM Seminars: season **2022**
http://www.ppgem.uerj.br

Introduction

The Hele-Shaw cell has been widely used as a low cost and highly effective experimental setup for the investigation of flow development in porous media, and reveals convective patterns occurring during flows driven by density gradients.

Fluid displacement development in porous media resembles finger-like projections and shows flow patterns which has also been referred to as dendrites. Dendrites growth phenomena occurring along convective displacements in porous media have been studied with the Hele-Shaw cell, where the Darcy law may be applied to explain fluid flow behaviour, provided that the solute hydrodynamic dispersion effect in the cell is taken into account.

Imary (1958) adopted a successful approach for providing derivation of the Darcy's law from the average of the Navier-Stokes equation with theoretical calculations. De Paoli et al. (2020) have shown experimentally that corrections can be applied to the Darcy equation to recover the additional solute hydrodynamic dispersion. Letelier et al. (2019) have shown theoretically and numerically that corrections can be applied to the Darcy equation to recover the solute spreading induced by the hydrodynamic dispersion. In this case, we are in the presence of a Hele-Shaw flow regime.

In this work, a Hele-Shaw cell apparatus is assembled to study flow pattern formation with fingering instability in density driven flows caused by the effects of chemical composition changes in fluid medium. The chemical composition change leads to a density increase on the surface, breaking vertical stability and disrupting buoyancy in the top layer of water, making it sink and originating fingers, as shown by the images obtained from the experiments carried out.

The Hele-Shaw flow equation can be obtained from the average of Navier-stokes momentum equation for in-compressible newtonian fluid as follows:

$$\rho\frac{D\mathbf{u}}{Dt} = -\nabla \mathrm{p} + \mu\nabla^2\mathbf{u} + \rho\mathbf{g} \tag{1}$$

where $\mathbf{u} = \mathbf{u}(x, y, z, t)$. For a thin gap, we assume that $\frac{D\mathbf{u}}{Dt} = 0$. Also, assuming a parabolic velocity profile

$$\mathbf{u}(x, y, z, t) = \frac{4}{b^2}\mathbf{v}_{max}(x, z, t)\, y(b - y) \tag{2}$$

The average velocity is

$$\mathbf{v}(x, z, t) = \frac{1}{b}\int_0^b \mathbf{u}(x, y, z, t)dy = \frac{2}{3}\mathbf{v}_{max}(x, z, t) \tag{3}$$

and considering a parabolic velocity profile across the cell gap

$$\mathbf{u}(x, y, z, t) = \frac{6}{b^2}\mathbf{v}(x, z, t)\, y(b - y) \tag{4}$$

Thus, the average of Navier-Stokes equation is employed to generate the Hele-Show flow equation:

$$\mathbf{v}(x, z, t) = -\frac{b^2}{12\mu}(\nabla p - \rho\mathbf{g}) \tag{5}$$

Materials and method

The diagonal configuration was chosen for the current experimental setup and the Hele-Shaw device remained open at the top boundary, where density gradients were triggered out by composition changes of the aqueous phase. Water was pumped until the compacted layer of potassium permanganate sitting on the top boundary was completely soaked.

After an initial diffusive phase, the layer of heavy mixture thickens, becomes unstable, and finger like structures form (Slim 2014). The development of coloured downward currents revealed the convective two-dimensional displacement patterns in porous media driven by concentration gradients.

The cell consisted of two rectangular ($27cm \times 20cm$) flat polycarbonate plates, 6 mm thick, separated by polyethylene tereftalate seals of 0.2 mm and c-clamps on three sides, enclosing three impenetrable boundary edges and a uniform gap. Since predictions made by

Figure 1: Fingering instability at $t = 90s$ (left), and $t = 360s$ (right).

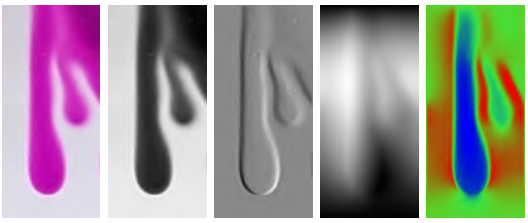

Figure 2: Reconstruction process (from left to right): image, concentration field c, $\frac{\partial c}{\partial x}$, ψ, and V_z.

the Darcy law become more accurate for smaller gaps, the experimental setup was designed with an adjustable and uniform gap ranging from 0.2 to 1 mm.

The dissolution process of potassium permanganate in the top layer of water in the cell was monitored and the evolution of the flow was captured by a camera recorder, as the Hele-shaw cell was illuminated by a light ring consisting of an array of LED lamps. Experimental data for flow velocity field was generated and concentration changes were observed.

Results and discussion

We assembled a Hele-Shaw tool specially designed for mimicking Hele-Shaw flows in porous media, and estimated three dimensionless parameter for the characteristic values of the problem. The Rayleigh number, that expresses relative strength of vertical advection and transverse diffusion, was $Ra = \frac{g\Delta\rho b^2 H}{12\mu D} = 1.4 \times 10^5$, whereas the anisotropy ratio, that scales the characteristic time of transverse difusion and longitudinal advection, was $\epsilon = \frac{b}{\sqrt{12}\,H} = 8.78 \times 10^{-5}$.

Finally, the combination of these two quantities gives a further dimensionless parameter, $\epsilon^2 Ra = 1.09 \times 10^{-1}$, and determines the flow behaviour (Letelier et al. 2019). When $\epsilon^2 Ra << 1$, we are in the presence of a Hele–Shaw flow regime and, therefore, the effect of dispersion has to be taken into account via corrective terms to the Darcy equation (Alipour et al., 2020).

The average velocity of the flow during the assays carried out was $0.5\,mm/s$ confirming previous estimates calculated with the Hele-Shaw equation; and showing that a single low frame rate camera can be used to record the development of the fluid flow patterns. The images obtained in figures 1 and 2 revealed the finger-like projections, a typical pattern of convective displacements driven by concentration gradients in porous media.

Further estimates for the concentration field and the derivative of concentration with respect to width dimension of the cell were obtained. Thus, vorticity across the gap dimension was worked out and the streamlines were obtained solving the laplacian of streamline function. Finally, the velocity component in the vertical direction was calculated, and figure 2 illustrates the steps of the process of velocity field reconstruction.

The investigation was carried out employing a quantitative photographic technique followed by post processing of the images, inferring density fields at high resolution from transmitted light intensity (Slim et al. 2013; Ching et al. 2017; De Paoli et al. 2020) Theoretical calculations with the Hele-Shaw equation fitted experimental data and showed that the tool accurately mimicked convective flow patterns in porous media.

Conclusion

In this work, a Hele-Shaw cell was designed for the experimental setup mimicking bi-dimensional fluid flow behaviour in porous media. Solute hydrodynamic dispersion played an important role and flow regime was described by the Hele-Shaw equation. Fingering instabilities were observed and tracking of chemical composition changes led to the reconstruction of the velocity field.

The Hele-Shaw cell revealed to be a safe, low cost, versatile tool and provided high quality experimantal data and benchmark results that can be used for validation of mathematical and computational models of pattern formation, and provide a better understanding of fluid displacement in porous media.

References

ALIPOUR, M.; De PAOLI, M.; SOLDATI, A. Concentration-based velocity reconstruction in convective Hele–Shaw flows. Experiments in Fluids, 61:195, p. 1-16, 2020.

BUNTON, P.; MARIN, D.; STEWART, S.; MEIBURG, E.; De WIT, A. Schlieren imaging of viscous fingering in a horizontal Hele-Shaw cell. Experiments in Fluids, 57:28, 2016.

MEHR, N,; ROQUES, C.; MÉHEUST, Y.; ROCHEFORT, S.; SELKER, J. Mixing and finger morphologies in miscible non-Newtonian solution displacement. Experiments in Fluids, 61:96, 2020.

OLIVEIRA, R.; MEIBURG, E. Miscible displacements in Hele-Shaw cells: Three-dimensional Navier–Stokes simulations. Journal of Fluid Mechanics, 687, 431-460, 2011.

THOMAS, C.; LEMAIGREA, L.; ZALTS A.; D'ONOFRIOC A.; De WIT A. Experimental study of CO2 convective dissolution: The effect of color indicators. International Journal of Greenhouse Gas Control, 42, p. 525-533, 2015.

De WIT, A. Chemo-hydrodynamic patterns in porous media. Phil. Trans. R. Soc. A 374: 20150419, 2016.

STUDY OF THE INFLUENCE ON AUTOGENOUS TIG WELDING PARAMETERS ON THE FAMILY OF DUPLEX STAINLESS STEEL

Author: Thaís de Paiva Menezes Viegas[1] *thais.viegas@cefet-rj.br*
Advisors: Marília Garcia Diniz[2]

[1] Federal Center for Technological Education of Rio de Janeiro
[2] Rio de Janeiro State University

May 15, 2022

PPG-EM Seminars: season **2022**
http://www.ppgem.uerj.br

Keywords: Welding; Duplex stainless steel, TIG welding, deleterious phases.

1 Introduction

The family of duplex stainless steels hold this nomination because the microstructure is constituted by balanced volume fractions of ferrite and austenite, resulting in structural materials with good mechanical and corrosion-resistance properties. Such properties ensure them a wide application in the chemical, petroleum and natural gas, and cellulose industries, among others. When exposed to high energy inputs, such as heat treatments, welding processes, or thermo-mechanical operations, an inbalance in the proportions of ferrite and austenite may occur, as well as the precipitation of deleterious phases, nitrites or carbides, leading to a weakening of the performances of these materials. The weldability of steels is always an important factor to be evaluated since it is the most common and often the only technique possible to be used for joining components. Welding processes usually involve sufficient heat input to cause microstructural changes in steels which are rich in alloying elements. The weldability of steels is always an important factor to be evaluated since it is the most common and often the only technique possible to be used for joining components. The objective of this research will be the evaluation of welded joints by autogenous TIG (Tungsten Inert Gas) process in order to identify the best welding parameters for some steels of the duplex family. An orbital TIG welding equipment will be built and metallographic characterization techniques, mechanical tests and corrosion tests will be used. As a result of this work, the best parameters for orbital autogenous of TIG welding for these steels will be suggested.

2 Methodology

The first stage of the project will be the construction of equipment for orbital welding, which will be carried out through the adaptation of a small mechanical lathe. The choice of a lathe is due to the ease of fixing a tubular part in it, which can be quickly performed with accessories for adaptation. A lathe is manufactured for machining parts and will be adapted for rotation that allows welding. Another adaptation will be the construction of a support for fixing the TIG welding gun on the lathe.

The second stage of the project will be the welding of duplex stainless steel specimens in the built equipment. Different specimens will be made, varying the parameters presented, like welding speed, pulsed and non-pulsed arc, welding frequency, amperage, workpiece to electrode distance, electrode type and shielding gas flow. The material for this work will be duplex tubes welded in an automated manner using the TIG process.

After making the specimens, the influence of each of the parameters will be analyzed on the microstructure, mechanical properties and corrosion resistance. Optical microscopy (OM), Scanning Electron Microscopy (SEM), Energy Dispersive Spectroscopy (EDS) and Atomic Force Microscopy (AFM) in Magnetic Force Mode (AFM-MFM) will be used to characterize the grain geometry in the melting zone and in the thermally affected, in addition to identifying the possible appearance of deleterious phases and nitrides. An EDS system coupled to the SEM will be used to identify the alloying elements present in each of the phases. Mass loss corrosion test according to ASTM G-48 will be conducted to quantify corrosion resistance. The mechanical properties of hardness and resistance will be verified by Vickers hardness tests and tensile tests in a universal machine.

3 Results

The influence of each of the parameters tested in the autogenous TIG welding process will be determined, as well as the best combination of these. And disseminate the results found through the publication of scientific articles, thus collaborating for the development of the welding industry in stainless steel, mainly benefiting the industries of the oil and gas sector. Establishment of partnerships with industries in the metal-mechanic sector of the State of Rio de Janeiro, due to the great interest in the subject by companies.

Figure 1 is a micrograph showing the transition region

from the base metal to the fusion zone of superduplex steel welded with autogenous TIG process. There is practically no Thermally Affected Zone. The chemical attack was done with the Behara reagent.

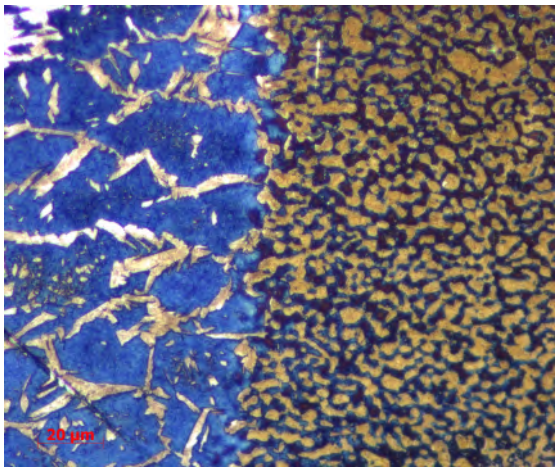

Figure 1: Transition region from base metal to fusion zone of superduplex steel welded with autogenous TIG process. The chemical attack was done with the Behara reagent.

At the end of the analysis, the best parameters for orbital autogenous TIG welding for these steels will be suggested.

4 Discussion and Conclusion

The main question with duplex steels is that the choice of the best parameters for autogenous welding wants to avoid, is the unbalance of phases, ferrite and austenite, and the emergence of deleterious phases, which cause loss of corrosion resistance.

The last stage of the work will consist of the analysis of the results obtained and the preparation of articles for publication. Science dissemination and popularization activities will also be carried out.

References

[1] Pimenta AR, Diniz MG, Perez G, Solórzano-Naranjo IG. Nitrogen addition to the shielding gas for welding hyper-duplex stainless steel. Soldagem e Inspeção. 2020; 25:1–8.

[2] Kumar S, Krisam S, Jacob A, Kiraly F, Keplinger A, Abart R, et al. Microstructures and element distributions in an aged hyper duplex stainless steel and corresponding hardness variation. Mater Des. 2020;194.

[3] Tavares SSM, Pardal JM, Ponzio E, Loureiro A, De Souza JA. Influence of microstructure on the corrosion resistance of hyperduplex stainless steel. Mater Corros. 2010;61(4):313–7.

[4] Pimenta AR, Estudo da Soldagem TIG em Aços Inoxidáveis Duplex e Construção de Equipamento para Soldagem Orbital, Projeto APQ 1; 2021.

[5] Menezes Viegas TP, Inspeção e Dimensionamento de Trincas em Superduplex; 2014.

[6] Villalobos Vera DI, Mendoza Bravo I. Effect of annealing temperature on the microstructure of hyperduplex stainless steels. Ing Investig y Tecnol. 2019; 20(2):1–6.

PPG-EM
Programa de Pós-graduação em Engenharia Mecânica

INHIBITION LAYER CHARACTERIZATION IN HOT DIP GALVANIZED SHEETS THROUGH DIGITAL IMAGE ANALYSIS AND PROCESSING.

Author: Arthur Werneck Ferreira[1] *ferreirawerneck@gmail.com*
Advisor(s): Marília Garcia Diniz[1]
[1] Rio de Janeiro State University

PPG-EM Seminars: season **2022**
http://www.ppgem.uerj.br
May 22, 2022

Keywords: Galvanization, inhibition layer, dross.

1 Introduction

The hot dip galvanizing process basically consists of inserting steel sheets into a bath of liquid zinc (Zn) at high temperature to form a protective coating against corrosion mechanisms. Due to this high temperature, part of the iron (Fe) contained in the steel is dissociated from it, combining with the zinc from the bath.

The junction of zinc and iron results in the formation of intermetallic phases composed of Fe-Zn with different chemical compositions. These phases adhere to the substrate surface in a stratified manner up to the top of the coating, where there is a phase, basically composed of zinc, called the "eta" phase. (η).

Figure 1 shows the cross section of a steel that has undergone the galvanizing process and identifies the main intermetallic phases formed between the substrate and the "eta" phase (η).

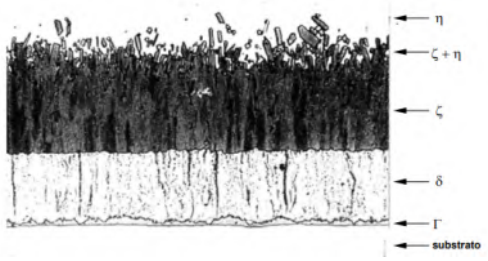

Figure 1: Cross-section of a hot-dip galvanized steel with an immersion time of one minute in a fluxing zinc bath at 450 ºC [1].

The formation of intermetallic phases is harmful to the zinc coating, as it will cause the phenomenon called powdering, in which the coating will not adhere to the steel. Especially when the process of mechanical forming of the coated sheets occurs, the tendency is for this coating to come off the substrate, which loses its protection against corrosion.

In order to avoid the formation of Fe-Zn phases small amounts of aluminum (Al) are added to the bath. For thermodynamic reasons, aluminum preferentially binds iron. A layer called "inhibitor layer" is then formed at the interface between the substrate and the coating, which is composed of Fe_2Al_5 particles. When Fe_2Al_5 particles are not found at the substrate/coating interface and, for some reason, lodge near the surface of the coating, a surface defect called Dross is created. This defect generates an undesirable surface appearance on the galvanized sheet.

The objective of this work was to identify and characterize the aspects of the inhibiting layer not defined as galvanized steel, considering the galvanizing parameters used in the process. In addition, we seek to find the presence of the Dross surface defect in the galvanized sheets.

2 Materials and Methods

The following steps were followed: cutting, embedding and metallographic preparation of an IF (Interstitial Free) steel sheet used by the automotive industry and which underwent the hot dip galvanization process.

Ten samples were embedded in conductive bakelite and metallographically prepared by sanding and polishing steps (hand sanding with a sequence of 220, 400, 600, 800 and 1200 mesh sandpaper and polishing with diamond paste with granulometries of 6, 3 and 1 m). Figure 2 shows some examples of steel samples that have been cut and some examples of samples already prepared and embedded in bakelite.

After metallographic preparation, the samples were sent for image capture through Optical Microscopy (OM) and Scanning Electron Microscopy (SEM). Chemical microanalysis using EDS (Energy Dispersive Spectroscopy) coupled to SEM.

3 Parcials Results

Figure 3 presents the result of the semi quantitative chemical analysis using EDS, where a false color mapping identified the regions containing Al particles by green. Note that the particles are concentrated between the substrate and the coating. According to the liter-

Figure 2: Some steel samples cut and some samples embedded in bakelite.

ature, this is the location for the Fe_2Al_5 phase and which characterizes the inhibitor layer [2] [3]. Faults were found in this layer.

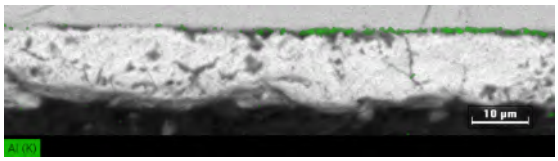

Figure 3: Chemical analysis of aluminum particles in galvanized sheet using EDS.

No particles that can be characterized as Dross were found until the present moment of this research.

4 Conclusions

The chemical analysis carried out using the EDS allowed the identification of the location of the aluminum particles. The location is consistent with where the inhibitor layer is (at the interface between substrate and coating). Thus, it is concluded that the aluminum particles identified are part of the Fe_2Al_5 phase, precisely the phase known as the inhibitory layer when it is in this location.

The analyzed samples did not present particles known as Dross.

5 Acknowledgments

This work was carried out with the support of the Coordination of Improvement of Higher Education Personnel Brazil (CAPES).

References

[1] MARQUES, Rodrigo José Alves. Avaliação da resistência à corrosão de aços IF revestidos com zinco e ligas de ferro-zinco destinados à indústria. Belo Horizonte, 2008.

[2] BREPOHL, Danielle Cristina Campos da Silva. Caracterização Das Camadas Formadas No Processo De Galvanização À Quente Sobre Uma Chapa De Aço Livre De Intersticiais. Curitiba, 2013.

[3] MANHABOSCO, Sara Matte. Avaliação do Comportamento Corrosivo De Aços Galvanizados Utilizando Microssondas Eletroquímicas. Porto Alegre 2017.

PPG-EM
Programa de Pós-graduação em Engenharia Mecânica

VERIFICATION OF ALE-FEM FOR CONVECTIVE DISSOLUTION OF CO_2 IN SALINE AQUIFERS WITH A MOVABLE SURFACE

Author: André Celestino Martins[1] *amartins2295@gmail.com*
Advisor(s): Norberto Mangiavacchi[1] and Rachel Manhães de Lucena[1]
[1] Rio de Janeiro State University

PPG-EM Seminars: season **2022**
http://www.ppgem.uerj.br
August 25, 2022

Keywords: Porous Medium, Convective Dissolution, ALE-FEM.

1 Introduction

According to the IPCC report [1], it is unequivocal that human influence contributes to an increase in the average temperature of the oceans, continents, and atmosphere. In this context, carbon capture and geological sequestration is the process of capturing carbon dioxide from large emission sources and redirecting it for storage in geological formations[3].

The conditions present in saline aquifer reservoirs, originates a CO_2-rich phase that is a mixture of brine and the CO_2 injected, and as the CO_2 is slightly soluble in the brine, it eventually diffuses into the original fluid [5]. Transferring mass from a solute to a fluid in porous layer through diffusion could provoke instabilities, and by the evolution of these, they will form finger-like structures, caused by the fluid with the dissolved solute that will be denser and therefore will sink, thus occurring a natural convection [2].

Thus, to study the phenomenon of convective dissolution of CO_2 in a saline aquifer through numerical simulation using the Finite Element Method with an arbitrary Lagrangian-Eulerian formulation (FEM-ALE), this work perform two verification methods for the developed computational code.

2 Mathematical model

The approach used to study the convective dissolution of CO_2 in the porous saline medium in this work is schematized in Fig. (1). The flow through the porous medium was considered two-dimensional, isothermal and with gravity being in the positive direction of the $y-$axis. In addition, the porous medium was supposed homogeneous, isotropic, inert, inertia was neglected, and the flow is single-phase.

In a similar way presented by Lucena et al. [4], the dimensionless continuity, Darcy, and concentration transport equations, respectively, were given by:

$$\nabla \cdot \mathbf{u} = 0, \tag{1}$$

$$\mathbf{u} = -\nabla p + c\mathbf{g}, \tag{2}$$

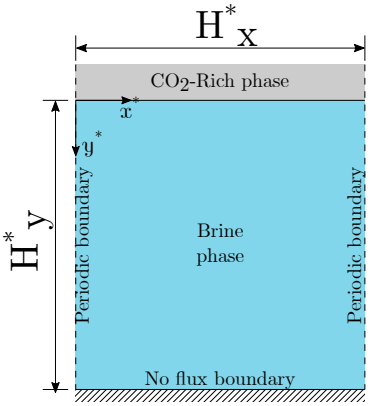

Figure 1: The model scheme proposed to study the phenomenon of convective dissolution of CO_2 in a saline aquifer.

$$\frac{\partial c}{\partial t} + \mathbf{u} \cdot \nabla c = \nabla^2 c. \tag{3}$$

As the original lengths of the porous medium are generally not relevant to the scale of the problem [5], using the chosen nondimensionalization is to be able to rewrite the width, $\mathcal{R}a_x$, and the length, $\mathcal{R}a_y$, of the medium as Rayleigh-Darcy number. The boundary conditions considered for the problem are given as follows:

$$c(x, y = 0, t) = 1, \tag{4}$$

$$\frac{\partial c}{\partial y}(x, y = \mathcal{R}a_y, t) = 0, \tag{5}$$

$$c(x = 0, y, t) = c\left(x = \mathcal{R}a_x, 0, t\right). \tag{6}$$

The initial conditions for the problem in the upper region and in the rest of the domain are given by, respectively:

$$c(x, y = 0, t = 0) = 1, \tag{7}$$

$$c(x, y > 0, t = 0) = 0. \tag{8}$$

3 Verification methods

To perform the verifications two different methods are proposed, transient 1D diffusion and the exponential growth of the eigenmodes of the linear stability analysis near a non-deformable surface.

3.1 Transient 1D concentration diffusion

The solution of Eq. (3), subject to boundary conditions Eqs. (4-6) and initial conditions Eqs. (7) and (8), is given by [5]:

$$\bar{c}(y,t) = 1 - \sum_{n=1}^{\infty} \frac{4}{(2n-1)\pi} e^{-[(2n-1)\pi/(2\mathcal{R}a_y)]^2 t} \times \sin\left(\frac{2n-1}{2\mathcal{R}a_y}\pi y\right). \quad (9)$$

The analytical solution of the problem is compared with the numerical solution made using the Finite Element Method (FEM), using two-dimensional triangular elements with linear base function, and and different mesh sizes.

3.2 Evolution of small concentration perturbations

To validate the implementation of the coupling between the pressure, velocity and concentration fields, for the case of a rigid surface, the results obtained can be compared with the Linear Stability Analysis (LSA) results. The methodology has already been detailed in Lucena et al. [4], and for linear stability analysis, was considered that the concentration and hydrodynamic profiles are equal to the sum of the base profiles, respectively, with perturbations. In this way, the equations can be rewritten as:

$$\begin{pmatrix} c \\ \psi \end{pmatrix} = \begin{pmatrix} \bar{c} \\ \bar{\psi} \end{pmatrix}(y,t) + \begin{pmatrix} \tilde{c} \\ \frac{i\tilde{\psi}}{k} \end{pmatrix}(y)\exp(\sigma t + ikx). \quad (10)$$

Manipulating and rearranging Eq. (10), the following eigenvalue problem is obtained:

$$\left[\bar{c}_y \left(D^2 - k^2\right)^{-1} k^2 - \left(D^2 - k^2\right)\right]\tilde{c} = -\sigma\tilde{c}. \quad (11)$$

The Eq. (11) was solved through the second-order central finite-difference method.

4 Results and Discussions

The result of the 1D transient concentration diffusion simulation, Fig. (2), showed a good agreement with the analytical solution of the problem. As expected, to meshes more refined the results are more accurate. Through the development of the LSA, Fig. (3), it is possible to verify the growth rates of perturbations for different instants of time and wavenumbers.

5 Conclusions

This work was an initial verification step to the developed code to perform the numerical simulations of the phenomenon of convective dissolution of CO_2 in saline aquifers using ALE-FEM. In future works, it is expected that the verified code will be able to represent and simulate the problem addressed well.

6 Acknowledgments

The authors acknowledge FAPERJ (Research Support Foundation of the State of Rio de Janeiro), CNPq (National Council for Scientific and Technological) and CAPES (Coordination for the Improvement of Higher Education Personnel) for their financial support.

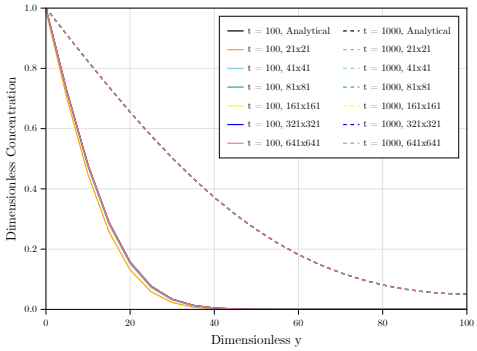

Figure 2: Dimensionless concentration profiles for $x = \mathcal{R}a_x/2$ for six different meshes in times $t = 100$ and $t = 1000$.

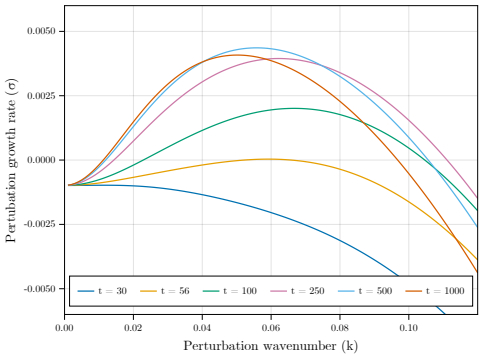

Figure 3: Perturbation growth rate as a function of wavenumber for different time instants.

References

[1] Richard P Allan, Ed Hawkins, Nicolas Bellouin, and Bill Collins. Ipcc, 2021: Summary for policymakers. 2021.

[2] Hamid Emami-Meybodi. Dispersion-driven instability of mixed convective flow in porous media. *Physics of Fluids*, 29(9):094102, 2017.

[3] Herbert E. Huppert and Jerome A. Neufeld. The fluid mechanics of carbon dioxide sequestration. *Annual Review of Fluid Mechanics*, 46(1):255–272, January 2014. doi: 10.1146/annurev-fluid-011212-140627.

[4] R.M. Lucena, J. Pontes, A. De Wit, G. R. Anjos, and N. Mangiavacchi. Linear stability analysis and nonlinear simulations of convective dissolution in an inclined porous layer between impermeable surfaces. *Chaos*, 2022. in press.

[5] Anja C. Slim and T. S. Ramakrishnan. Onset and cessation of time-dependent, dissolution-driven convection in porous media. *Physics of Fluids*, 22(12): 124103, December 2010. doi: 10.1063/1.3528009.

MICROSTRUCTURE AND DENSIFICATION OF HYDROXYAPATITE TABLETS OBTAINED FROM PRESSED AND SINTERIZED FISH SCALE

Author: Camila Alves Pelicarto da Silva Botão[1] *silva.camila$_1$@posgraduacaouerj.br*
Advisor(s): José Brant de Campos[1]
[1] Rio de Janeiro State University

October 21, 2022
PPG-EM Seminars: season **2022**
http://www.ppgem.uerj.br

Keywords: Pirarucu scales, Hydroxyapatite, Biomaterials; Ceramic processing.

1 Introduction

Hydroxyapatite (HAp) is ceramic with bioactive, biocompatible and osteoconductive properties, characteristics that make its use increasingly advantageous in several areas. Apatite has a chemical similarity to parts of the human body such as bone tissue and dental tissue [1]. With a stoichiometric compound of Ca/P ratio equal to 1.67 and form $Ca_{10}(PO_4)6OH_2$, HAp is formed by apatite $Ca_{10}(PO_4)_6X_2$ plus the OH- radical that replaces the anion X^-[2]. HAp can be classified in two ways, natural, which is found in the mineral phase of calcium- deficient bone tissue, and synthetic, which are produced in laboratories and may have a precursor of organic origin (chicken eggshell, beef bone and scale fish) or a synthetic precursor [3]. With its wide applicability, new synthesis routes have become necessary as well as the use of new sources of precursors for the production of HAp [4]. At the same time, 4% of the tons of fish waste discarded annually refer to fish scale, which can be used in the cosmetics and pharmaceutical industry in the production of collagen and HAp [5]. Thus, the present work aimed to verify the effects of heat treatment on the microstructure and densification of pressed and sintered tablets at 1000°C of HAp produced from Pirarucu fish scale.

2 Methodology

The procedure applied to the present work consisted of pressing, sintering and characterization steps. The HAp used for the production of pressed and sintered tablets were produced under two different conditions: sample of HAp powder that did not undergo heat treatment (Green) and HAp powder that was heat treated at 1000°C for 5 h. Both samples used Pirarucu scale as a precursor, following the precipitation synthesis route.

For pressing the samples, a uniaxial hydraulic press from PUCRio was used. The applied load was 5 tons for 30 seconds with a matrix of metallic origin with 16 mm in diameter and 7 inserts were produced for each condition with a final thickness of 4 mm, totaling 14 inserts. After pressing, the tablets were sintered at 1000°C for 2h in a muffle furnace brand Quimis model Q318M21 belonging to Universidade Estácio de Sá Campus Maracanã.

- Measurements of density, apparent porosity and densification

In order to determine the apparent density, water absorption, porosity and densification presented by Button et.al [5] three tablets of each condition were submitted to the Archimedes method, following the ABNT NBR 16661 (2017) standard, using a scale of precision (0.0001g) BEL brand with accessory for measuring density from the Ceramics Laboratory of IME.

- Scanning Electron Microscopy (SEM)

The Scanning Electron Microscopy (SEM) technique presented by Button et.al [5] used the following scanning conditions: LED detector, acceleration voltage 2kV, emission current 95.4 ηA, probe Current 6 and vacuum $9.6E^{-5}Pa$. The analysis was performed to verify the morphology of the powder before pressing and the microstructure after sintering the tablets. The equipment used was from the manufacturer JEOL JSM-7100F from the Multiuser Laboratory of Nanofabrication and Characterization of Nanomaterials (NanoFAB) at the University of the State of Rio de Janeiro (UERJ).

3 Results

3.1 Measurements of density, apparent porosity and densification.

Measurements of density, apparent porosity and densification were obtained using the Archimedes Method. Analyzing three sintered specimens of each condition according to ABNT NBR 16661 (2017). As can be seen in the table above, the Thermally treated HAp presented higher values for porosity and lower values for apparent density and densification, expected values because once the powder is thermally treated at high temperature before sintering, there is a decrease in energy the which causes a decrease in the growth rate of the grain forming agglomerates and thus part with a

Table 1: table of measurements of apparent density, apparent porosity and densification

	Green HAp	Heat treated HAp
Density A.	$2,98 \pm 0,03 g/cm^3$	$2,43 \pm 0,01 g/cm^3$
Porosity	$1,07 \pm 0,034\%$	$17,4 \pm 0,07\%$
Densification	$94,43 \pm 1,01$	$77,88 \pm 0,32$

greater porosity.

3.2 Scanning Electron Microscopy (SEM)

The green HAp powder particles (Fig. 1A) are smaller than the heat treated HAp particles (Fig. 1B), proving that heat treatment at 1000°C for 5h favored particle growth.

Figure 1. HAp powder A)Green B)Heat treated at 1000°C for 5 hours.

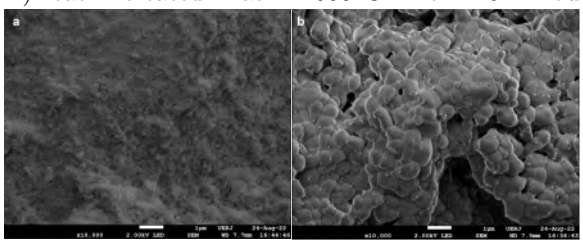

An increase in particle size can also be seen in Fig. 2 after sintering producing homogeneous coaxial grains similar to the microstructure found by Huang et. al, (2011) [6] who studied HAp obtained from Tilapia scale and heat treated at 800°C for 4h.

Figure 2. Sintered tablets at 1000°C for 2 hours A)Green and B)Heat treated.

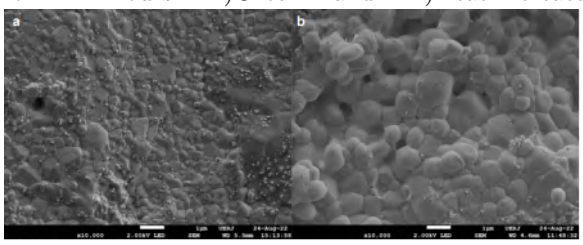

4 Conclusions

From the above results we can reach the following conclusions:

- The Green HAp tablets, because they contain smaller particles, presented a greater densification, favoring the thermodynamic processes of surface energy decrease;
- The heat treated samples before sintering were analyzed from the apparent density and through SEM images and showed higher porosity and lower densification;
- The agglomeration of larger particles generated by the heat treatment at high temperature confirmed greater amounts of pores in the parts;

Samples not heat treated prior to sintering are more suitable for applications where densified samples are required. However, when it comes to cell anchoring, where porosity is a relevant property, heat treatments prior to sintering associated with other porous materials processing techniques are more suitable for such application.

References

[1]Santos, M. L.; Florentino, A. O.; Saeki, M. J.; Aparecida, A. H.; Fook, M. V. L.; Guastaldi, A. C. (2005), Síntese de hidroxiapatita pelo método sol-gel utilizando precursores alternativos: nitrato de cálcio e ácido fosfórico. Eclética Química. FapUNIFESP (SciELO). http://dx.doi.org/10.1590/s0100-46702005000300004.

[2] Kumar, A.; Negi, Y. S.; Choudhary, V.; Bhardwaj, N. K. (2014), Microstructural and mechanical properties of porous biocomposite scaffolds based on polyvinyl alcohol, nano-hydroxyapatite and cellulose nanocrystals. Cellulose. Springer Science and Business Media LLC. http://dx.doi.org/10.1007/s10570-014-0339-7.

[3] Aguilar, M. S.;. Campos, J. B; Di Lello, B. C.; Queiroz, F.; Campos, N. C.(2014), Síntese de hidroxiapatita com o uso de carbonato de cálcio de origem biológica como precursor.21° CBECIMAT - Congresso Brasileiro de Engenharia e Ciência dos Materiais 09 a 13 de Novembro de 2014, Cuiabá, MT, Brasil.

[4]Santos, M. L.; Florentino, A. O.; Saeki, M. J.; Aparecida, A. H.; Fook, M. V. L.; Guastaldi, A. C. (2005), Síntese de hidroxiapatita pelo método sol-gel utilizando precursores alternativos: nitrato de cálcio e ácido fosfórico. Eclética Química. FapUNIFESP (SciELO). http://dx.doi.org/10.1590/s0100-46702005000300004.

[5] Botão, C. A. P. S., Baêta Júnior, E. S.; Aguilar, M. S.; Moura, F. J.; Aguilera, L. S.; Campos, J. B. (2022),Microestrutura, densificação e microdureza de pastilhas de hidróxiapatita obtida a partir de escama de peixe prensadas e sinterizada. 13° ECTM- Encontro de Ciência e Tecnologia de Materiais 20 a 21 de outubro de 2022, Brasil.

[6] Huang, Y-C.; Hsiao, P-C.; Chai, H.-J. (2011), Hydroxyapatite extracted from fish scale: effects on mg63 osteoblast-like cells. Ceramics International. Elsevier BV. http://dx.doi.org/10.1016/j.ceramint.2011.01.018.

PPG-EM
Programa de Pós-graduação em Engenharia Mecânica

WEAR RATE AND HARDNESS IN BIODEGRADABLE POLYMERIC MATRIX COMPOSITES (PBAT)

Author: Frederico GB Lacerda[1] *fredbindi@gmail.com*
Advisor(s): Marília G Diniz[1]
[1] Rio de Janeiro State University

Aug 22, 2022

PPG-EM Seminars: season **2022**
http://www.ppgem.uerj.br

Keywords: PBAT; Biodegradable composite; Hardhness; Abrasion.

1 Introduction

The degradation of the environment by human action has driven the search for solutions compatible with socioeconomic growth. In addition to recycling, a universal response to waste disposal, the use of biodegradable materials that can be decomposed by microorganisms normally present in the soil is promising [2].

Poly (butylene adipate-co-terephthalate) (PBAT) is a synthetic polymer that has high elongation before breaking, which makes it suitable for use in biodegradable films, packaging and coatings, as it is a copolyester that degrades completely in a few weeks with the help of natural enzymes from the environment, being even allowed for applications in food packaging by the Food and Drug Administration (FDA) because it is a polymer totally free of heavy metals. It also has good processability and mechanical properties similar to low-density polyethylene films [2]. However, the mechanical properties of these are often inferior compared to many commonly used petroleum-based polymers. The biodegradability of PBAT alone is not sufficient for the acceptance of this material. High production costs and low thermo-physical and mechanical tensile strength, when compared to non-biodegradable polymers, are obstacles that make it difficult to use this material in some situations [3].

The incorporation of nano and micro-scale fillers can significantly improve the mechanical, thermal and dimensional performance of biodegradable polymers. The challenge lies in dispersing the nanoreinforcement in the matrix, which is a key factor in improving the polymer properties [5]. The addition of reinforcements to renewable polymer matrices has been shown to be a good alternative, providing an improvement in the properties of the matrix polymer, also obtaining low-cost biodegradable materials [7].

The objective of this study was to characterize the Shore D hardness and wear rate for different types of composites with nano and micro scale reinforcements in PBAT polymer matrix. The characterization of this property for pure PBAT was also performed.

2 Methodology

The materials used were virgin PBAT biodegradable polymer matrices, with a density of 1.26g/cm^3, Ecoflex from OEKO Bioplásticos, nanometric cellulose (nCE) CelluForce NCC from CelluForce and microcrystalline cellulose (mCE) from Viafarma.

A concentrate (masterbatch) containing 20% m/m filler was prepared in a single-screw extruder with three heating zones: 140°C, 150°C and 160 °C at 60 rpm. After this step, the material was pelleted for further mixing with the virgin polymer.

From the processed material, laminates measuring 11cm x 11cm, 1.5mm thick, were obtained by compression molding in a Carver hydraulic press, model 3851-0, with heating at 160ºC for 6 minutes at 4,000psi. For cooling, a Carver cooled hydraulic press, model C, was used for 6 minutes at 4,000psi (Table 1).

Table 1: Characteristics of the samples.

Sample	fillers	% m/m
PBAT	-	-
PBAT-nCE1	nanocellulose	1
PBAT-nCE3	nanocellulose	3
PBAT-nCE5	nanocellulose	5
PBAT-mCE1	microcellulose	1
PBAT-mCE3	microcellulose	3
PBAT-mCE5	microcellulose	5

Twelve Shore D hardness measurements were performed for each sample using a Shore D durometer, model HT-6510D from [1]. All measurements were performed at room temperature and at random positions.

For the abrasion test, the mass losses during the abrasive tests and the specific masses for all composites were quantified, in order to quantify the volume losses of the materials.

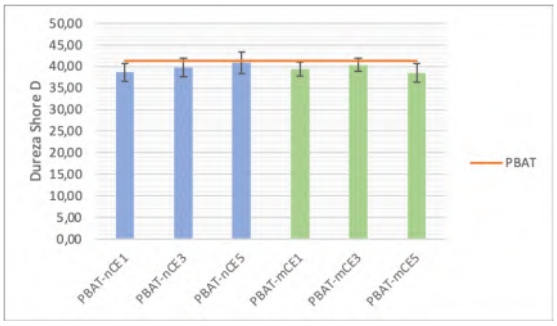

Figure 1: Average of the Shore D hardness.

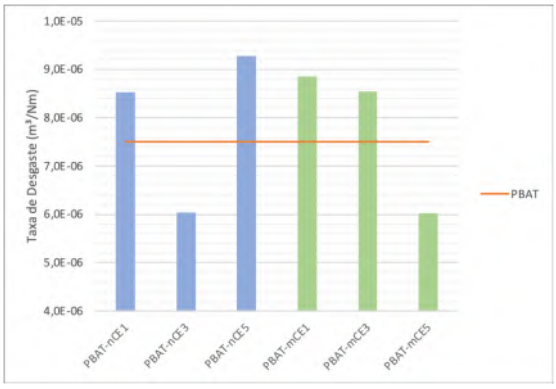

Figure 2: Wear rates (Ws) by abrasion.

The equipment used was a drum abrasimeter brand VEB model APGi 613.10. Three samples of each composite were used, in addition to pure PBAT. The drum was coated with 2000 mesh grit sandpaper and always changed for each new sample. The number of cylinder rotations was 40 ± 1 RPM and the load used was 500gf (4,905N). For each sample, the abrasion path was covered 10 times.

The respective mass values of each sample were recorded before (m0) and after (mf) the test, using a Marte model AY220 scale, with a precision of 0.0001g.

For wear modeling, the densities of each composite were determined by the hydrostatic method, according to ASTM D297:15.

3 Results

All average hardness of composites with nano and microfillers (Figure 2) showed a decrease in relation to pure PBAT. A Student Hypothesis T test with 95% reliability [6] revealed that the addition of cellulosic fillers did not significantly influence the average hardness of composites when purchased with pure PBAT.

Compared to pure PBAT, the abrasion wear rates showed an increase in the presence of microfillers with 1 and 3% m/m and a decrease with 5% m/m, this variation may suggest that with the percentage increase of the load to higher values than 3%, wear rates will decrease. With nanofillers, higher values of wear rate were obtained with 1 and 5% m/m, and a drop with 3% m/m, which shows that nanofillers led to differences in wear behavior when compared with microfillers. , since the load distribution is different (Figure 2).

It is known that polymeric materials do not have a standard for mechanical behavior like metals, and that the degree of load dispersion in composites is a determining factor for obtaining improved properties [4]. The results obtained here in the hardness and abrasion tests were probably influenced by the dispersion of cellulosic fillers in the PBAT.

4 Conclusions

The data obtained in the hardness tests revealed that the PBAT was not influenced by the addition of loads. Compared to pure PBAT, abrasion wear rates decreased with 5% m/m microfiller and 3% m/m nanofiller. These values can be considered as the optimal percentages for the application of nano and micro fillers in the studied polymer. Both the abrasion and hardness results were probably influenced by the dispersion of cellulosic fillers in the PBAT.

When comparing wear and hardness results, it is not possible to obtain a direct correlation.

5 Acknowledgments

The author thanks all the teachers, the advisor M.G. Diniz, PPG-EM/UERJ for their support, laboratory colleagues, and Faperj for funding the study.

References

[1] ASTM D 2240:2015 e1. Standard test method for rubber property - durometer hardness. Technical report, ASTM - American Society for Testing and Materials, 2015.

[2] M.B.C.; Almeida T.G.; Bardi M.A.G.; Carvalho L.H.; Canedo E.L. Falcão, G.A.M.; Vitorino. Pbat/organoclay composite films: preparation and properties. *Polymer Bulletin, Springer*, 1, 2017.

[3] L.S.; Gouveia R.F.; Lona L.M.F. Ferreira, F.V.; Cividanes. An overview on properties and applications of poly(butylene adipate-co-terephthalate)-pbat based composites. *Polymer Engineering Science*, 1, 2017.

[4] Friedrich Klaus. *Friction and Wear of Polymer Composites*. Hamburg Polymer Composites Group, 1984.

[5] S.K. Mohanty, S.; Nayak. Biodegradable nanocomposites of poly(butylene adipate-co-terephthalate) (pbat) and organically modified layered silicates. *J Polym Environ. Springer*, 1, 2012.

[6] G.C. Montgomery, D.C.; Runger. *Applied Statistics and Probability for Engineers*. John Wiley Sons, 2020.

[7] F.S.; Rosa D.S. Silva, C.G.; Kano. Thermal stability of the pbat biofilms with cellulose nanostructures/essential oils for active packaging. *Journal of Thermal Analysis and Calorimetry*, 1, 2019.

PPG-EM
Programa de Pós-graduação em Engenharia Mecânica

FINITE ELEMENT SIMULATION OF TEMPERATURE DISTRIBUTION ON THE HEAD SKIN SURFACE

Author: Leib de Andrade Neubarth[1] *leib999@yahoo.com.br*
Advisor(s): Norberto Mangiavacchi, Gil Roberto Vieira Pinheiro [1]
[1] Rio de Janeiro State University

PPG-EM Seminars: season **2022**
http://www.ppgem.uerj.br
September 01, 2019

Keywords: temperature distribution, finite element simulation, head temperature, COVID-19

1 Introduction

Numerical simulations and experiments can be employed in the development of robust and efficient tools to support avoidance and reduction of contamination of the SARS-CoV-2 virus. Accurate measurement of skin surface temperature at the head, and in particular, in the face, can be employed as screening method to check for possible infection by virus such as Covid-19. In this work a methodology, based on numerical simulations employing the Finite Element Method (FEM) and experimental results, is developed to obtain robust and efficient tools to support avoidance and reduction of virus contaminations. We propose the development of improved thermographic systems to evaluate human body temperature in collective agglomerations with high fluxes of people. The developed numerical methods allow to simulate the temperature distribution on the skin surface under various conditions, thus allowing a deeper understanding and analytical capability to interpret sensor data and IR imagery. The model's results, validated and combined with experimental data, will be employed in future works to feed AI based monitoring systems.

2 Problem description

A geometric model of the head surface is employed to generate the 3D computational model of the head. The head interior is the domain Ω, and it's surface is divided in the boundaries Γ_1 and Γ_2, as shown in Fig.(1).

The following assumptions were made to model the problem:

- Steady state;
- Uniforme internal heat source in Ω;
- In Ω the heat transferred by conduction;
- In Γ_1 the heat is transferred by convection;
- In Γ_2 there is no heat transfer.

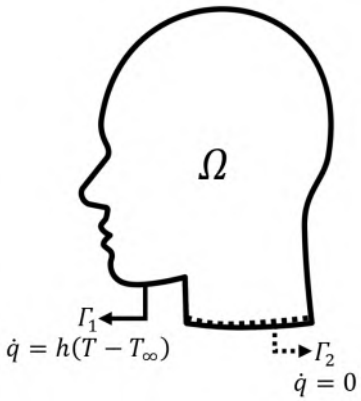

Figure 1: Problem description

3 Equations

The steady state solution of the heat equation in the domain Ω is given by:

$$-\nabla \cdot K\nabla T = S \ \ at \ \ \Omega \tag{1}$$

subject to boundary conditions

$$-K\nabla T\cdot = h(T - T_\infty) \ \ at \ \ \Gamma_1 \tag{2a}$$
$$-K\nabla T\cdot = 0 \ \ at \ \ \Gamma_2 \tag{2b}$$

To perform the nondimensionalisation, the following variables and parameters are defined:

$$\xi = \frac{x}{L_0} \tag{3a}$$
$$T_{ref} = \frac{SL_0^2}{K_0} \tag{3b}$$
$$u = \frac{T - T_\infty}{T_{ref}} \tag{3c}$$
$$\kappa = \frac{K}{K_0} \tag{3d}$$
$$Bi = \frac{h\,L_0}{K_0} \tag{3e}$$

Using the dimensionless variables (3a) to (3e), the problem can be expressed as

$$-\nabla \cdot \kappa\nabla u = 1 \ \ at \ \ \Omega \tag{4}$$

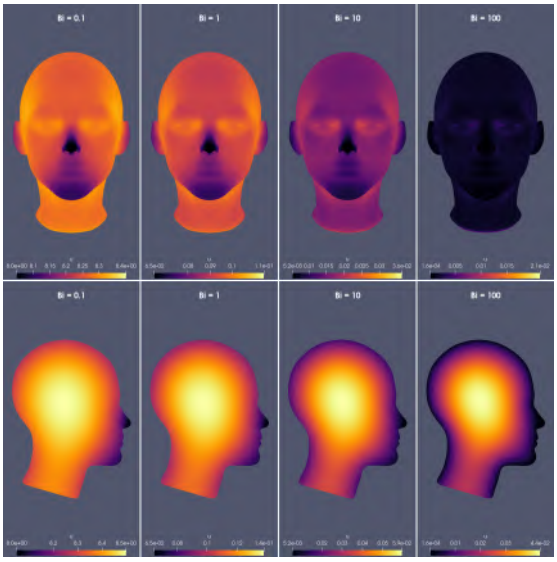

Figure 2: Surface and cross-section non-dimensional temperature for $Bi = 0.1, 1, 10$ and 100

subject to boundary conditions

$$-\kappa \nabla u \cdot = Bi\, u \;\; at \;\; \Gamma_1 \tag{5a}$$

$$-\kappa \nabla u \cdot = 0 \;\; at \;\; \Gamma_2 \tag{5b}$$

To solve the dimensionless equations (4), (5a) and (5b) using the Finite Element Method, the equations must be put in the weak form. It can be formulated as:

$$\kappa \int_\Omega \nabla u \cdot \nabla v \, d\Omega + Bi \oint_{\Gamma_1} uv \, d\Gamma_1 = \int_\Omega v \, d\Omega \tag{6}$$

Using Gridap [1, 3] - a Julia [2] library for FEM simulations - the weak form (6) can be solved numerically.

4 Results

Simulations were run using $Bi = 0.1, 1, 10$ and 100 to resemble varied wind regimes. They can be seem in Fig.(2). The same geometric surface model is also employed in the fabrication of a physical model by additive manufacturing with a Sethi BB FDM 3D printer, using polylactic acid (PLA) filament. Tests were conducted using the 3D printed model. To simulate the internal heat generation, a 40W incandescent light was turned on inside the model, and the model was allowed to warm up for 10 minutes. To obtain the thermal images, a Flir E75 Thermal Imaging Camera is used, with a 320 x 240 (76,800 pixels) IR Resolution, Thermal Sensitivity/NETD $<$ 0.03C@30C(86F), and Spectral Range 7.5 – 14.0 m. These results showed that relative greater temperatures were found around the eyes, neck, nape and temples in all simulations. Similarly, the temperature of the nose, lips, chin and ear edges were cooler. Such regions have great agreement to those observed in the conducted physical experiment, as in Fig. (3).

5 Conclusions

Simulations were performed using many Biot numbers to estimate different wind conditions. Despite the simplified heat generation model, the simulation was able

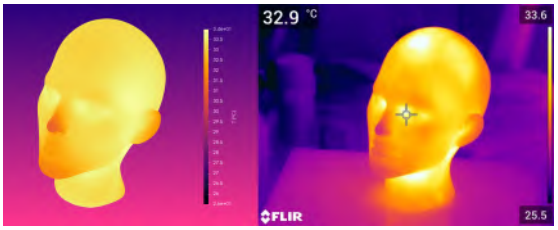

Figure 3: Comparison between simulation (left) and thermal image of 3D printed heated model (right).

to predict the hottest and coolest regions in the head. In future works, the convective heat transfer h will be estimated using an external CFD simulation coupled with heat transfer.

6 Acknowledgments

The author thank FAPERJ (Research Support Foundation of the State of Rio de Janeiro), CNPq (National Council for Scientific and Technological Research), and CAPES (Coordination for the Improvement of Higher Education Personnel) for their financial support.

References

[1] Santiago Badia and Francesc Verdugo. Gridap: An extensible finite element toolbox in julia. *Journal of Open Source Software*, 5(52):2520, 2020.

[2] Jeff Bezanson, Alan Edelman, Stefan Karpinski, and Viral B. Shah. Julia: A fresh approach to numerical computing. *SIAM Review*, 59(1):65–98, 2017.

[3] Francesc Verdugo and Santiago Badia. The software design of gridap: A finite element package based on the julia JIT compiler. *Computer Physics Communications*, 276:108341, July 2022.

PPG-EM
Programa de Pós-graduação em Engenharia Mecânica

INFRARED CHARACTERIZATION OF RECYCLED POLYAMIDE FROM TEXTILE WASTE

Author: Petterson Borges Machado[1] *petterson.machado@iff.edu.br*
Advisor(s): José Brant de Campos[1]
[1] Rio de Janeiro State University

PPG-EM Seminars: season **2022**
http://www.ppgem.uerj.br
Sep 08, 2022

Keywords: Polyamide, Textile waste, Recycling, Thermal analysis.

1 Introduction

Industries in general, including textiles, are looking for more efficient, economical and sustainable processes to avoid harming the environment. According to the Brazilian Textile and Apparel Industry Association, Abit, in 2020 Brazil produced 7.93 billion pieces (clothing + socks and accessories + bed, table and bath) and 1.91 million tons. So much potential in the textile industry results in the generation of approximately 160 thousand tons of waste per year in the country [1].

Today, many textile products are made from pure synthetic yarns or blends with natural yarns. Among synthetic polymeric fibers, polyamide fibers are among the most used and are considered the noblest of synthetic fibers, due to their characteristics of high mechanical strength, elasticity, softness, lightness and shine, and it can be used in a variety of applications [2].

For this reasons, to control and for the application these materials, this work presents a methodology to process and to reuse the residues of polymeric fibers (polyamide) from textile industries. In addition, it seeks to understand structural characteristics of this polymer to provide parameters and procedures adopted during its reprocessing. The FTIR test (Fourier Transform Infrared Spectroscopy) was used and it is presented in this work to evaluate the functional present in the sample and to validate the presence of polyamide in the recycled material. The knowledge of characteristics and of the processing variables would let the application of, such a polymer with better performance and use of its properties (mechanical, chemical), and control the products obtained from this polymeric material.

2 Experimental

2.1 Material

The polymeric waste used in the present study was supplied by a company in the field of women's underwear in the city of Nova Friburgo – RJ. These wastes are made up of microfiber scraps.

The microfiber used is from the advance brand with a composition of 87 percent polyamide and 13 percent elastane. After collecting the discarded products, the tissue was separated and placed in a metallic container for its melting The material was heated to a temperature close to 300º C, above the melting temperature of the material, until all the material was fused. Later, after the complete fusion of the tissue, it was immediately spread over a marble stone at room temperature and it returned to a solid state. However it was possible to observe a change in its mechanical behavior. Previously the material has presented a highly elastic behavior but, after passing the cooling step it has started to behave like a hard and brittle material.

Subsequently, this material was subjected to a ball milling process. The material grounded was placed inside a cylindrical drum which has a rotation between 4 and 20 revolutions per minute. The product was mixed and powdered by grinding (alumina balls with an average diameter of 4 cm) as a result of the rotation. After 24 hours of grinding, we obtained a very fine powder, which passed through a 1mm sieve, ensuring that the granulometry of the powder obtained is less than this value. Figure 1 shows the processing steps of Fabric (Microfiber) placed in the pan (a), Fabric completely fused (b), stiffened tissue (c), Result of grinding (d).

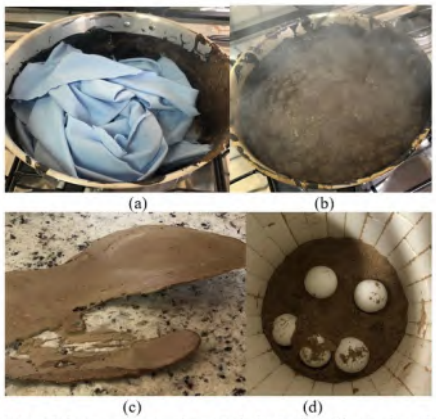

Figure 1 – Material processing - (a) – Fabric (Microfiber) placed in the pan; (b) – Fabric completely fused; (c) stiffened tissue; (d) Result of grinding

2.2 Fourier transform infrared spectroscopy (FTIR)

FTIR spectroscopy analyzes were performed using the Thermo Electron Corporation Nicolet-520 G spectrophotometer. The spectrum of the mesh sample was obtained with a resolution of 2 cm^{-1}, in the spectral range of 4000 to 700 cm^{-1}.

Fourier Transform Infrared Spectroscopy (FTIR) is a technique for the characterization of polymers for identification and/or determination of structural characteristics of polymers, functional groups and bonds presented in the sample.

3 Results and Discussion

3.1 Fourier transform infrared spectroscopy (FTIR)

Figure 2 shows the FTIR spectrum of the polyamide-elastane microfiber mesh. The infrared absorption bands that characterize polyamides are observed at 3300 cm^{-1} relative to the vibrations of asymmetric axial stretching of the free [N-H] group, 3078 cm^{-1} relative to the folding of the [N-H] group, 2941 cm^{-1} and 2863 $^{-1}$ referring to the asymmetric and symmetrical stretching [C-H] in CH2, respectively, 1639 cm^{-1} due to the stretching of the [C=O] group of the primary amide, 1544 cm^{-1} due to the folding of the group [N-H] and [C-N] stretching of the secondary amide, 930 cm^{-1} due to [C-CO] stretching, at 731 cm^{-1} referring to the balance of [CH_2] relative to the folding of the [N-H] group [4,5].

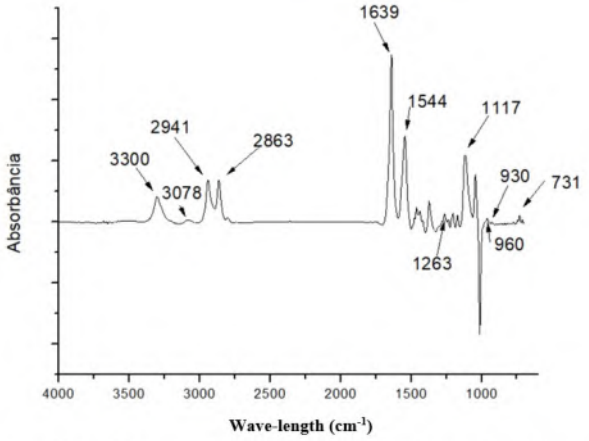

Figure 2 - Infrared absorption spectra of polyamide 6 microfiber mesh with elastane.

In Brazil, type 6 or 6.6 polyamide fiber and filament yarns are produced and consumed, and according to [6] the infrared absorption spectra of the polyamides clearly differ in the region below 1350 cm^{-1}, where the variations in the absorption bands can be related to the direction of the CO-NH functions and to the parity in the amount of CH_2 groups. The differentiation between these two polymers according to [4] and [6] occur in the bands observed at 1263 cm^{-1} referring to the balance of [CH_2], 1117 cm^{-1} due to the stretching of the groups [C-C and CO-NH], 960 cm^{-1} referring to the stretching [CO-NH], which are bands in positions characteristic of polyamide 6. Polyamide 6, with an odd number of CH_2 groups, is characterized by the absence of the band corresponding to 1220 cm^{-1}, and by the absence of bands at 1140 cm^{-1} and 1273 cm^{-1}, which are absorption bands in positions characteristic of polyamide 6.6 due to the alternating orientation of the [CO-NH] functions.

From the identification of spectral bands and comparison of the spectrum obtained from the microfiber mesh of polyamide with elastane with ASTM D276, the bands observed are characteristic bands of polyamide 6, in agreement with the work of [7].

4 Conclusions

The microfiber was processed in order to observe and understand structural characteristics of this polymer to provide parameters and procedures to be adopted during its reprocessing through FTIR analysis.

The FTIR analysis allowed us to observe that there is polyamide in the analyzed sample, due to the bands analyzed, especially bands with characteristics of polyamide 6, as expected.

In general, it can be said that there was a confirmation of the presence of polyamide 6 in the recycled material that was processed. These results indicate the potential for application of this recycled material in uses where polyamide 6 is required.

References

[1] ABIT - Associação Brasileira da Indústria Têxtil e de Confecções (2022) – Disponível em: <https://www.abit.org.br/cont/perfil-do-setor>. Acessado em: 01 ago. 2022.

[2] MAKHLOUF, C.; LADHARI, N.; BRAHAM, D.; ROUDESU, S.; SAKLY, F. The improvement in dyeing properties of modified polyamide 6.6 microfibers with a cationic dye. International journal of applied research on textile, v. 3, n. 1, p. 44-57, 2015.

[3] MAKHLOUF, C.; KACEM, C.; ROUDESLI, S.; SAKLI, F. Dyeing behaviour of unmodified and polyamide 6.6 fibers of different levels of fineness. Journal of applied sciences, v. 8, n. 1, p. 77-85, 2008.

[4] ENLOW, E. M et al. Discrimination of nylon polymers using attenuated total reflection mid-infrared spectra and multivariate statistical techniques. Journal of Applied Spectroscopy, v. 59, n. 8, p. 986-992, 2005.

[5] PAVIA, D. L. et al. Introdução à espectroscopia. Ed. 2, São Paulo: Cengage Learning, 2015.

[6] GUILLÉN, J. A. Métodos de indentificación de las diferentes fibras poliamídicas. Boletín Intexter del Instituto de Investigación Textil y de Cooperación Industrial, n. 20, p. 11-21, 1964.

[7] LUNA, C. B. B. et al. Reactive processing of PA6/EPDM-MA blends as modifier for application and development of high-performance polypropylene. Journal of Vinyl and Additive Technology, v. 27, n. 4, p. 736-756, 2021.

PPG-EM
Programa de Pós-graduação em Engenharia Mecânica

POOL FIRE AND THERMAL RADIATION HEAT FLUX MODELING USING CFD

Author: Marcelo André Cordeiro da Silva[1] *silva.marceloac@gmail.com*
Advisor(s): Norberto Mangiavacchi[1]
[1] Rio de Janeiro State University

April 19, 2022
PPG-EM Seminars: season **2022**
http://www.ppgem.uerj.br

Keywords: CFD, FDS, pool fire, thermal radiation heat flux modeling.

1 Introduction

The storage of liquid fuels in surface tanks is a typical activity in several installations, like oil refineries, fuel terminals, and general industries. Gasoline is one of the most stored fuels. This kind of storage offers a risk of fire due to several causes such as tank leakage and fuel ignition, which can cause pool fire, flash fire and fireball. The fire in a vertical cylindrical tank is classified as a pool fire. In a pool fire, convection currents act shaping the flame, under the influence of turbulence factors. A fraction of the heat generated is emitted in the form of thermal radiation. The impact of this radiative heat flux in a body is greatly influenced by the geometric relationship between the flame and the irradiated body. When an human body is the receptor from a fire radiative heat flux, certain level of radiation can cause 1st, 2nd or 3rd degree burns, causing minor, moderate or severe injuries or even death [6]. A risk analysis that has a pool fire scenario usually takes into account the value of second degree burn (5 $\mathrm{kW/m^2}$), and the radiation values to probabilities of death calculated through probit functions. This paper aims to present a method of measuring the intensity of thermal radiation as a function of the distance from pool fires. Safe distances from pool fire considering impact of the heat flux by radiation were found.

2 Methodology

The methodology applied in this work consists in simulate pool fire scenarios to analyse and predict safety distances using Computation Fluid Dynamics (CFD). For this study it was used CFD program Fire Dynamics Simulator (FDS); Smoke View (SMV), a program used to view FDS simulations; Pyrosim, a graphical user interface for FDS and Smoke View and; Matlab. Some FDS simulation results were used to compute, using Matlab, safety distance values from fire.

2.1 Mathematical model

The FDS mathematical models include hydrodynamic model [4] and [3], combustion model and thermal radiation model [2] and [4] to simulate fire. Probit equation [1] was applied to find safety distance relative to 1% probality of human death due to thermal radiation from fire.

2.1.1 Hydrodynamic model

$$\frac{\partial \rho}{\partial t} + \nabla \cdot \rho \mathbf{u} = 0 \tag{1}$$

$$\rho \left(\frac{\partial \mathbf{u}}{\partial t} + \frac{1}{2} \nabla |\mathbf{u}|^2 - \mathbf{u} \times \omega \right) + \nabla p - \rho \mathbf{g} = \nabla \cdot \sigma \tag{2}$$

$$\rho c_p \left(\frac{\partial T}{\partial t} + \mathbf{u} \cdot \nabla T \right) - \frac{dp_0}{dt} = \dot{q} + \nabla \cdot k \nabla T \tag{3}$$

$$p_0(t) = \rho R T, \tag{4}$$

2.1.2 Combustion model

$$\dot{q}_c'' = \Delta H_o \frac{dY_o}{dZ} (\rho D) \nabla Z \cdot \mathbf{n}; Z < Z_f, \tag{5}$$

2.1.3 Thermal radiation model

$$\mathbf{s} \cdot \nabla I_\lambda(\mathbf{x}, \mathbf{s}) = \kappa_\lambda(\mathbf{x}) [I_b(\mathbf{x}) - I_\lambda(\mathbf{x}, \mathbf{s})], \tag{6}$$

It was employed a gray gas model for the radiation absorption coefficient (FDS default), a function of gas composition and temperature according to [5].

2.1.4 Probit equation

$$Pr = -36.38 + 2.56 \ln (Q^{4/3} t), \tag{7}$$

where, Pr is the probit corresponding to the probality of death; Q ($\mathrm{W/m^2}$) is the heat radiation and t(s) is the exposure time, with maximum value of 20 s.

2.2 Models and Simulations

In this work, two pool fire cases were modeled and simulated with gasoline fuel:

1. Case Study I - pool fire in a vertical cylindrical tank without wind and;
2. Case Study II - pool fire in a vertical cylindrical tank with wind.

2.3 Radiation estimation method

In order to analyse the fire hazards, the radiative heat transfer was computed at several points using the FDS device named "Radiative Heat Flux Gas". In these points, the "Radiative Heat Flux Gas" devices were applied, thus establishing one mesh of evaluation points for the incident radiative heat flux for all simulations. At each point, the radiation was computed for 26 different directions, simulating the presence of 26 radiometers pointing out each one to a different direction. The directions are symmetrically distributed in order to capture the incident radiation in each one. All simulated radiometers are located at a height of 1.70 m from the ground level.

3 Results

The pool fire Case Studies I and II were runned in FDS to simulate 60 s of fire. The Figure 1 shows simulations at time $t = 30$ s. The results obtained from FDS for the radiation in Case Studies I and II were processed using Matlab program to give the maximum distance reached by the radiative heat flux from pool fire at the levels of interest. The levels of interest are 5 kW/m^2, capable of causing second degree burn, and 9.8 kW/m^2, corresponding to the probit of death probability of 1%, according to Eq.(7). The safety distances from pool fires scenarios using the method adopted to estimate radiative heat flux equal to 5 kW/m^2 and 9.8 kW/m^2 are shown in Tab. 1. These distances are given by the largest distance reached by the corresponding contour curves, measured from the center of the tank.

Table 1: Distances from pool fires to radiative heat flux of interest.

	C. Study I	**C. Study II**
Fuel Volume	248.41 m^3	248.41 m^3
Wind Speed	0.00 m/s	4.00 m/s
Wind Direction	-	0°
5 kW/m^2	-	11.20 m
9.8 kW/m^2	-	-

4 Conclusions

The application of CFD is shown to be a viable and advantageous method for providing more realistic results for fire modeling and simulation. It can be concluded that the use of CFD provides relevant information for the analysis of risk of injury and death of people due to fires in installations that store or process flammable and combustible substances.

5 Acknowledgments

The author would like to acknowledge INEA, UERJ, Thunderhead Engineering, FAPERJ, CNPq and CAPES.

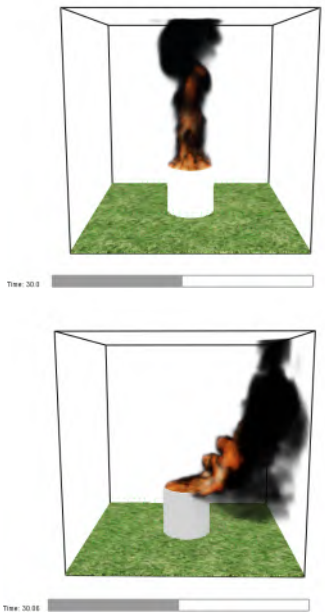

Figure 1: Smoke View figures from pool fire simulations in FDS to Case Study I (up) and II (down) at simulation time $t = 30$ s. View in Case Study II are rotated to improve visibility.

References

[1] *Guidelines for Quantitative Risk Assessment - CPR 18E Part One: Establishments - "Purple Book".*

[2] S. Hostikka, K. McGrattan, and A. Hamins. Numerical modeling of pool fires using LES and finite volume method for radiation. In *Proceedings of the Seventh International Symposium on Fire Safety Science. International Association for Fire Safety Science, Pp 383-394*, Worcester, MA, 2003. International Association for Fire Safety Science.

[3] K. McGrattan, H. R. Baum, and R. G. Rehm. Large eddy simulations of smoke movement. *Fire Safety Journal*, 30:161–178, 1998.

[4] K. McGrattan, S. Hostikka, R. McDermott, J. Floyd, and M. Vanella. *Fire Dynamics Simulator Technical Reference Guide Volume 1: Mathematical Model.* NIST - National Institute of Standards and Technology and VTT Technical Research Centre of Finland, 2018.

[5] K. McGrattan, S. Hostikka, R. McDermott, J. Floyd, and M. Vanella. *Fire Dynamics Simulator User's Guide.* NIST - National Institute of Standards and Technology and VTT Technical Research Centre of Finland, 2018.

[6] U. M. Niazi, M. S. Nasif, M. B. Muhammad, and M. Imran. Modelling of pool fire and injury prediction considering different wind speeds and directions in offshore platform. *ARPN Journal of Engineering and Applied Sciences*, 11:13000–13005, 2016.